Author/s:
Blades, F;Chambers, JD;Aumann, TD;Nguyen, CTO;Wong, VHY;Aprico, A;Nwoke, EC;Bui, BV;Grayden, DB;Kilpatrick, TJ;Binder, MD

Title:
White matter tract conductivity is resistant to wide variations in paranodal structure and myelin thickness accompanying the loss of Tyro3: an experimental and simulated analysis

Date:
2022-07-01

Citation:
Blades, F., Chambers, J. D., Aumann, T. D., Nguyen, C. T. O., Wong, V. H. Y., Aprico, A., Nwoke, E. C., Bui, B. V., Grayden, D. B., Kilpatrick, T. J. & Binder, M. D. (2022). White matter tract conductivity is resistant to wide variations in paranodal structure and myelin thickness accompanying the loss of Tyro3: an experimental and simulated analysis. Brain Structure and Function, 227 (6), pp.2035-2048. https://doi.org/10.1007/s00429-022-02489-8.

Brain Structure and Function
https://doi.org/10.1007/s00429-022-02489-8

ORIGINAL ARTICLE

White matter tract conductivity is resistant to wide variations in paranodal structure and myelin thickness accompanying the loss of Tyro3: an experimental and simulated analysis

Farrah Blades[1,5] · Jordan D. Chambers[2] · Timothy D. Aumann[1] · Christine T. O. Nguyen[3] · Vickie H. Y. Wong[3] · Andrea Aprico[1] · Eze C. Nwoke[1] · Bang V. Bui[3] · David B. Grayden[2] · Trevor J. Kilpatrick[1] · Michele D. Binder[1,4]

Received: 16 December 2021 / Accepted: 25 March 2022

Abstract

Myelination within the central nervous system (CNS) is crucial for the conduction of action potentials by neurons. Variation in compact myelin morphology and the structure of the paranode are hypothesised to have significant impact on the speed of action potentials. There are, however, limited experimental data investigating the impact of changes in myelin structure upon conductivity in the central nervous system. We have used a genetic model in which myelin thickness is reduced to investigate the effect of myelin alterations upon action potential velocity. A detailed examination of the myelin ultrastructure of mice in which the receptor tyrosine kinase Tyro3 has been deleted showed that, in addition to thinner myelin, these mice have significantly disrupted paranodes. Despite these alterations to myelin and paranodal structure, we did not identify a reduction in conductivity in either the corpus callosum or the optic nerve. Exploration of these results using a mathematical model of neuronal conductivity predicts that the absence of Tyro3 would lead to reduced conductivity in single fibres, but would not affect the compound action potential of multiple myelinated neurons as seen in neuronal tracts. Our data highlight the importance of experimental assessment of conductivity and suggests that simple assessment of structural changes to myelin is a poor predictor of neural functional outcomes.

Keywords Myelin · Action potential · Conduction · Paranode · Mathematical modelling

Introduction

Myelin enables efficient, saltatory conduction of neural signals in the vertebrate central nervous system (CNS) (Huxley and Stämpfli 1949). Myelin enhances the speed of signal conduction by neurons, both by altering the physical parameters of the axonal membrane such as resistance and capacitance, and by inducing clustering of sodium channels at short unmyelinated sections of the axons known as nodes of Ranvier [reviewed in Lubetzki et al. (2020)]. Axon myelination can increase the velocity of axonal signal conduction tenfold compared with an unmyelinated axon of the same calibre (Waxman and Bennett 1972). Moreover, there is clear evidence that myelination is responsive to environmental changes and learning, by the formation of new myelin segments (internodes) and by adjustments to the thickness and length of the myelin that ensheaths axons (Chang et al. 2016). In demyelinating diseases such as multiple sclerosis (MS), newly generated myelin is often observed to be thinner than in equivalent undamaged regions (Duncan et al. 2017). It is therefore critical to understand the changes in conductivity that arise from the alterations to the structure of the myelinated axon unit to predict the functional consequences of myelin modifications in both health and disease.

✉ Michele D. Binder
mbinder@florey.edu.au

1 The Florey Institute of Neuroscience and Mental Health, University of Melbourne, Parkville, VIC 3010, Australia

2 Department of Biomedical Engineering, University of Melbourne, Parkville, VIC 3010, Australia

3 Department of Optometry and Vision Sciences, University of Melbourne, Parkville, VIC 3010, Australia

4 Department of Anatomy and Physiology, University of Melbourne, Parkville, VIC 3010, Australia

5 Present Address: Centre for Solar Biotechnology, Institute for Molecular Biosciences, University of Queensland, St Lucia, QLD 4072, Australia

Published online: 19 April 2022

There are numerous methods for the prediction of conduction velocity in response to changes in myelin ultrastructure. In 1952, Hodgkin and Huxley generated a series of equations to enable the prediction of conduction velocities based on alterations in ion channel composition, temperature, and axonal diameter (Hodgkin and Huxley 1952). However, these equations were defined using giant squid axons, which are not only non-mammalian but are not myelinated. In an important and influential paper, Waxman (1980) combined empirical data and theoretical modelling to describe the influence of various parameters on nerve conduction, including myelin thickness, fibre diameter, and internode length (Waxman 1980). Waxman showed that, for a given axon diameter, conduction velocity is highly dependent upon myelin thickness (Waxman 1980). However, experimental confirmation of the predicted effect of myelin thickness upon conduction velocity is relatively limited and not always in accordance with prediction. For example, Smith et al. (1979) showed in a cat model of demyelination, that remyelination of spinal cord fibres resulted in the restoration of secure conduction with a conduction velocity indistinguishable from control, despite the persistence of thinner myelin sheaths (Smith et al. 1979). To complement these findings, it has also been shown that the cat optic nerve restores near-normal latencies in visual-evoked potentials (VEP) following remyelination, despite the presence of thinner than normal myelin (Heidari et al. 2019).

The discordance of modelled changes in conduction velocity compared with experimental data highlights the importance of direct electrophysiological assessment of the result of structural changes in myelin. Here, we use the Tyro3 deficient mouse to both experimentally document and mathematically model the effect of alterations to myelin upon axonal conduction velocity in white matter tracts. The hypomyelinated phenotype of Tyro3 deficient mice is well defined in both the central and peripheral nervous systems (Miyamoto et al. 2015; Akkermann et al. 2017; Blades et al. 2018). We undertook a detailed examination of the ultrastructure of myelinated axons in the absence of Tyro3. We found that the loss of Tyro3 results in disruption to the paranode, but did not result in overt changes to the node of Ranvier. Surprisingly, despite these structural changes, we did not observe any alterations to experimentally measured action potential velocities in the corpus callosum or the optic nerve. We then developed a mathematical model to explore the effects of altering myelin parameters in either single fibres or populations of fibres. Using this model, we found the input of parameters derived from our Tyro3-deficient mouse predicted a decrease in conduction velocity in single fibres, but not in fibre populations. Our results suggest that changes to myelin ultrastructure do not necessarily result in changes in conduction velocity in fibre tracts, and that single fibre measurements may not adequately reflect global effects on action potential conduction.

Materials and methods

Animals

Tyro3 knockout (KO) mice were derived from an in-house colony that were previously backcrossed onto the C57Bl/6 background and housed in a specific-pathogen-free environment during all experimentation and breeding. Mice were housed in littermate groups prior to experimentation. Following VEP implantation, mice were single-housed for 1 week to facilitate recovery from the surgical procedure. All animal procedures were performed in accordance with the Florey Institute of Neuroscience and Mental Health animal care committee regulations. Experimental cohorts consisted of Tyro3$^{+/+}$ littermates [denoted as wild-type (WT)] which were used as controls and Tyro3$^{-/-}$ mice (denoted as Tyro3 KO). Mice were age and sex matched for each genotype. All experimentation in this study was performed in adult mice (8–12 weeks of age).

Transmission electron microscopy (TEM)

To evaluate myelin paranodal loop structure, we employed high-power transmission electron microscopy (TEM). Mice were anaesthetised with 100 mg/kg sodium pentobarbitone (Virbac, Milperra, Australia) and perfused with 4% paraformaldehyde (PFA). Whole optic nerves were dissected and incubated in Karnovky's solution overnight at 4 °C, and then stored in 0.1 M sodium cacodylate. Tissue was then post-fixed in 1.5% ferrocyanide and 1% osmium tetroxide to visualise myelin prior to embedding in Spurr's resin. Optic nerves were cut longitudinally to visualise paranodal loops and images captured using a JEOL-1400 Flash TEM (JOEL Ltd., Akishima, Tokyo, Japan) at 4000 to 15000× magnification. Nodes were deemed in plane if paranodal loops were visible at the top and bottom of the same internode, and ≥ 20 paranodal regions were captured per mouse ($n = 6$ per genotype). Structural integrity of paranodal loop regions was manually assessed with Fiji software [NIH ImageJ v1.52p (Schindelin et al. 2012)]. Paranodal loops were classified as disrupted if any myelin loops were inverted, detached, and everted, if there was interloop separation or if the loop contained abnormal debris. Results are presented as % disrupted nodes per mouse, with group ($n = 6$ per genotype) data given as mean ± standard error of the mean (SEM).

Fluorescent immunohistochemistry

Adult mice were anaesthetised as described above and perfused intracardially with 1% PFA. Optic nerves and whole brains were dissected and embedded in optimum cutting temperature compounds (Sakura Finetek, Tokyo, Japan). Optic nerves were orientated longitudinally and brains coronally. For assessment of nodes within the corpus callosum, 7 µm sections were cut using a cryostat as close to Bregma 0.98 as possible and mounted on SuperFrost™ glass slides (Invitrogen, Thermo Fisher Scientific, Carlsbad, CA). Prior to use, slides were equilibrated to room temperature (RT) and rehydrated in PBS. Non-specific binding was blocked using 10% normal goat serum with 0.3% Triton X-100 (blocking buffer) for 1 h at RT. Tissue was then incubated with primary antibody mouse IgG1-anti-pan sodium ion channel (pan Na_V; 1:100; #S8809, Sigma-Aldrich, St-Louis, MO, USA) for at least 12 h at 4 °C. Slides were washed in PBS for 5 min three times (denoted as washed) and then incubated with secondary antibody, donkey anti-rabbit-647 (1:200; #711-075-152, Jackson ImmunoResearch Laboratories, West Grove, PA, USA) for at least 1 h at RT. Slides were again washed, and then incubated with rabbit-anti-contactin-associated protein [(Caspr); 1:200; #AB34151, Abcam, Cambridge, UK] and mouse IgG2b-anti-potassium ion channel 1.2 (K_V1.2; 1:200; #75–008, NeuroMab, Davis, CA, USA) for at least 3 h at RT. Slides were then washed and incubated with goat-anti-mouse IgG1-488 (1:200; #115–545-205, Jackson ImmunoResearch Laboratories) and goat-anti-mouse IgG2b-594 (1:200; #115–585-207, Jackson ImmunoResearch Laboratories) for at least 1 h at RT.

Slides were mounted with fluorescent mounting medium (DAKO, Glostrup, DK). Tissue was visualised using a Zeiss LSM 780 confocal microscope (Carl Zeiss AG, Oberkochen, DE) at 63× magnification [63X/1.4 oil lens (PL-APO)]. Using Zen Black software (SP5; Carl Zeiss, AG), images were captured as z-stacks (~0.8 µm increments). Nodal lengths were measured when all three nodal markers were in plane. Measurements were performed manually using Fiji software [NIH ImageJ v1.52p, NIH ImageJ (Schindelin et al. 2012)]. The length of nodes of Ranvier was defined as the distance between Caspr-positive paranodes. Results are presented as mean node length per mouse, with group data ($n = 6$ mice per genotype) given as mean ± SEM.

Compound action potentials (CAPs)

CAPs were measured in adult Tyro3 KO and WT mice (n = 12 per genotype). Mice were deeply anaesthetised via isoflurane inhalation, decapitated and the head placed into artificial cerebrospinal fluid (ACSF; 125 mM NaCl, 25 mM $NaHCO_3$, 3 mM KCl, 1.25 mM $NaH_2PO_4{\cdot}H_2O$, 2 mM $CaCl_2$, 1 mM $MgCl_2$, 25 mM glucose, pH 7.4) at 0 °C for dissection (a slurry of crushed ACSF ice and ACSF liquid). Brains were carefully removed, adhered to a vibratome cutting platform with superglue, and submerged in ACSF at 0 °C for sectioning. Brains were sectioned coronally at 300 µm using a vibratome (Integraslice 7550 MM, Campden Instruments, Leicestershire, UK). Cell metabolism was normalised for 1 h by incubating slices in 37 °C ACSF infused with 95% oxygen and 5% carbon dioxide. For recording, a slice was taken from the normalisation bath and placed in an experimental chamber under a microscope (DMLFSA, Leica Microsystems, Wetzlar, DE) within a Faraday cage. Within the experimental chamber, slices were continuously perfused with oxygenated ACSF (1 mL/min) and maintained at 22 °C. Axons in the corpus callosum were electrically stimulated extracellularly with a concentric bipolar electrode (#CBBRF75, FHC, Bowdoin, ME, USA) and compound action potentials (CAPs) were recorded with a glass micropipette containing internal solution (144 mMK-Gluconate, 3 mM $MgCl_2.6H_2O$, 10 mM HEPES, 0.5 mM EGTA pH 7.2, osmolarity 290, resistance 6 MOhm). Stimulating and recording electrodes were initially placed close together (~150 µm apart) along with a common bundle of callosal fibres (visualised using differential interference contrast optics at × 40 magnification) and CAP responses to 10 constant current electrical simulation pulses (biphasic, 100–300 µA at 0.2 ms/phase, 2 s separation) were recorded extracellularly. Measurements were also taken at greater distances between stimulating and recording electrodes along the same 'beam' of stimulated axons in each slice. This procedure was carried out on slices located from bregma − 0.5 to 0.16. Each of the ten pulses of the CAP reading was averaged and normalised for analysis using Clampfit (v10.1; Molecular Devices LLC, San Jose, CA, USA). N1 (primary negative deflection) and N2 (secondary negative deflection) were manually determined as the minimum of the respective deflection. Stimulating and recording electrode distances were then manually measured using Fiji software [NIH ImageJ v1.52p, NIH ImageJ (Schindelin et al. 2012)]. Conduction velocities (CVs) were calculated by dividing distance between stimulating and recording electrodes by the time to either the N1 or N2 deflection, with the mean conduction velocity determined for each mouse. The half-width (duration at 50% maximum amplitude) of N1 and N2 were measured for all deflections where both the onset and end of the deflection could be determined. All data are shown as mean ± SEM.

Visual-evoked potentials (VEPs)

VEPs were recorded in adult Tyro3 KO and WT mice to assess electrophysiological function of the visual system in the absence of Tyro3. The VEP reflects the functional integrity of visual pathway including the eye, optic nerve,

optic tract, lateral geniculate nucleus, optic radiations, and occipital cortex. Alterations at any stage along the visual pathway, including the optic nerve, can manifest as alterations to the VEP (Holder 2004; Vidal-Jordana et al. 2021). Eight-week old Tyro3 KO ($n = 10$) and WT ($n = 10$) mice were anesthetised with isoflurane (induction 3–3.5%, with oxygen at a flow rate of 3 L/min, maintenance 1.5% isoflurane with oxygen at 2 L/min) and stainless-steel screws [1 mm × 3 mm, DCS-PH103 pan head screws sterilised with chlorhexidine (DCCconcepts Ltd, North Yorkshire, UK)] were implanted into the cranium, contacting the dura matter but not penetrating or damaging the cortical tissue. The implanted screws acted as measuring electrodes for the electrical activity of the visual cortices. Active electrodes were implanted into the left and right visual cortices at 3 mm caudal bregma, 3 mm lateral to the midline. A reference electrode was implanted 1 mm rostral to bregma. After the placement of electrodes, dental amalgam was spread over the cranial bone to stabilise the electrodes for recordings. Following electrode implantation surgery, mice were given 7 days to recover before recordings were undertaken. VEP active and inactive electrodes were fastened with alligator clips. Electrical current was grounded by a subcutaneously inserted, stainless-steel needle electrode (F-E2-30, Grass Telefactor, AstroMed, RI, USA) placed into the animal's tail. To maintain corneal hydration and electrical conductance, gel lubricant was added to the electrodes (10 mg carmellose sodium, Celluvisc, Allergan, Gordon, NSW, AU), as necessary. VEPs were recorded using diffused light stimuli across a range of luminous energies (0.72–2.07 log cd s/m^2). Light was emitted by an array of eight white LEDs (8 Watt Luxeon LED, Lumileds Lighting Company, CA, USA). LEDs were embedded inside a Ganzfeld sphere (Photometric Solutions International, Oakleigh, VIC, AU) placed in front of the animal with the eyes positioned at the front of the sphere. VEP signals were acquired from both visual cortices simultaneously at a 4 kHz acquisition rate with pre-amplifier (P511, Grass Telefactor, Astro-Med) and hardware band-pass filter settings of 0.1–100 Hz (− 3 dB). Signals were then digitised (ML785 Powerlab 8SP, ADInstruments Pty Ltd., Bella Vista, NSW, AU) and recorded using Scope software (ADInstruments Pty Ltd.). Analyses were performed in Excel (v16.0 Microsoft Corporation, Redmond, Washington, WA, USA) where the N1 and P2 amplitude and implicit times were extracted. All data are shown as mean ± SEM.

Computational modelling of conduction velocity

A previously published model of a single axon was used to model CAPs (Richardson et al. 2000; Bakiri et al. 2011; Arancibia-Cárcamo et al. 2017). In brief, a single axon was modelled as a series of connected nodes and internodes. The nodes included conductance parameters for three different voltage-gated channels, namely, fast Na_V, persistent Na_V, and slow K_V. The internode region was divided into multiple compartments to represent the paranode and juxtaparanode, where the number of compartments remained large (10–70) for accurate simulation (Arancibia-Cárcamo et al. 2017). The specific myelin conductance and myelin capacitance of the internodes was determined by the number of myelin wraps, width of the periaxonal space, axon diameter, and length of the paranode (Bakiri et al. 2011). The differential equations for the nodes and internodes were derived using Kirchhoff's Current Law and solved using implicit numerical integration (Halter and Clark 1991). A mathematical model of CAPs was produced to assess the functional outcomes of myelin abnormalities observed in the Tyro3 KO mouse. The CAP was modelled as a combination of single axons

$$\mathrm{CAP} = \frac{1}{N}\sum_{i=N} a_i.v_i(x), \tag{1}$$

where a_i represents the distance between the axon and recording electrode, $v_i(x)$ is the membrane potential determined by the single axon model for an input vector x, and $N = 400$ is the number of single axon models used to estimate the CAP. We used 400 axons to simulate the CAP as it was enough axons to produce smooth and consistent CAP whilst maintaining a manageable number of CPU hours required to simulate the CAP. The input vector, x, defines the axon diameter, node length, internode length, g-ratio, number of myelin wraps, and periaxonal space. For the CAP, the parameters for each axon (axon diameter, node length, internode length, and g-ratio) were generated independently. Random number generators were used to produce the properties of each of the 400 axons. Depending upon the modelling paradigm, in some simulations, the same seed for the random number generators was used, which ensured all axons had the same random properties over multiple simulations except for the parameters that were being investigated. For the purposes of the model parameters were generated using a method which produces a normal distribution, which may not exactly represent real-world data which are more likely to be a complicated combination of Poisson and normal distribution, since there is a limit on the lower end, but no limit on the higher end. The numerical values for axon diameter, g-ratio, and myelin lamellae were set to match the experimentally recorded values for the Tyro3 KO and WT (Table 1). All other parameters in the single neuron model remained at the default values from the previous model designed for the corpus callosum (Bakiri et al. 2011). The distance between each axon and the recording electrode, a_i, was also assumed to be normally distributed.

The simulations were performed using MATLAB (Mathworks, Natick, MA, USA). An action potential in the single neuron model was evoked by current injection (3 mA for

Table 1 Numerical values for parameters investigated

Parameter (units)	CAP model WT Mean ± standard deviation (experimental value)	CAP model Tyro3 KO Mean ± standard deviation (experimental value)
Node diameter (μm)	0.6 ± 0.15	0.6 ± 0.15
Node length (μm)	1 ± 0.1	1 ± 0.1
Internode diameter (μm)	0.72 ± 0.18 (0.6)	0.72 ± 0.18 (0.77)
Internode length (μm)	79 ± 7.9	79 ± 7.9
g-ratio	0.704 ± 0.07 (0.703)	0.724 ± 0.07 (0.727)
Number of myelin wraps	5.41 ± 1.6 (5.39)	4.92 ± 1.5 (4.83)
Periaxonal space (nm)	5.45 ± 1.4 (5.53)	5.45 ± 1.4 (5.5)

The numerical values for parameters used to simulate the WT CAP and Tyro3 KO CAP (Fig. 6a). The means and standard deviations were used to normally distribute the values for single axons in the CAP. The experimental value indicates the mean value measured in our experiments. All other parameters in the single neuron model remained at the default values of the previous model of the corpus callosum (Bakiri et al. 2011)

10 μs) at the first node. The recording electrode was placed 0.75 mm from the start of the first node. The number of nodes and internodes was the minimum number required to reach the recording electrode for the given values of lengths of the nodes and internodes.

Statistical analysis

Statistical analyses were performed using GraphPad PRISM 8 (v8.4.1, GraphPad Software, San Diego, CA, USA). Differences between genotypes of a single continuous variable were assessed using unpaired Student's t tests. Welch's corrections were employed when SDs differed between groups. Differences between genotypes for two category variables (paranodal loop faults) were assessed using Chi-square tests. An α of 0.05 was used to define statistical significance.

Code accessibility

A MATLAB implementation of the single axon model was downloaded from https://github.com/AttwellLab/MyelinatedAxonModel. The code/software described in the paper is freely available online at https://github.com/JordanChambers/compound-action-potential.

Results

Tyro3 deficiency is associated with structural abnormalities at CNS paranodes

It has previously been shown that myelin is thinner in the absence of Tyro3 in both the CNS and the PNS independent of any alteration in the density of myelinated axons, raising the possibility that action potential conduction would be adversely affected by the reduction in myelin thickness (Miyamoto et al. 2015; Akkermann et al. 2017; Blades et al. 2018). As the nodal and paranodal structure is also intimately linked with action potential propagation, we investigated the ultrastructure of the paranode in both the corpus callosum and optic nerve of Tyro3 KO mice and compared them with WT controls. Representative images of paranodes from the optic nerves of WT and Tyro3 KO mice are shown in Fig. 1a, b. In the absence of Tyro3, we observed multiple paranodes with structural faults such as loop detachments and inversions compared with WT controls in both the corpus callosum and the optic nerve. The optic nerve was used for quantification of these faults, as more in-plane paranodes could be identified in this tissue compared to the corpus callosum. To quantify disruptions to paranodal loop regions, we assessed paranodal loop faults of the Tyro3 KO and WT group as outlined in the schematic in Fig. 1c and quantified in Fig. 1d. Paranodes were considered disrupted if they contained at least one fault. Consistent with previous findings (Bull et al. 2014), we show that, in adult WT mice, around 35% of paranodal loops appear to have one or more paranodal loop faults (Fig. 1d). The loss of Tyro3 was associated with significantly more disrupted paranodal loops (Fig. 1d; 35.19 ± 5.94% vs. 72.06 ± 10.29% disrupted nodes, WT versus Tyro3 KO respectively, $p < 0.0001$).

The length of the node of Ranvier is not altered in the absence of Tyro3

We next assessed whether the paranodal disruptions identified above altered the distribution of sodium channels at the node of Ranvier. Nodes were identified by immunofluorescent detection of potassium channels (juxtaparanode), Caspr (paranode), and sodium channels (node) (Fig. 2a). Only nodes with sodium channels between adjacent Caspr-positive

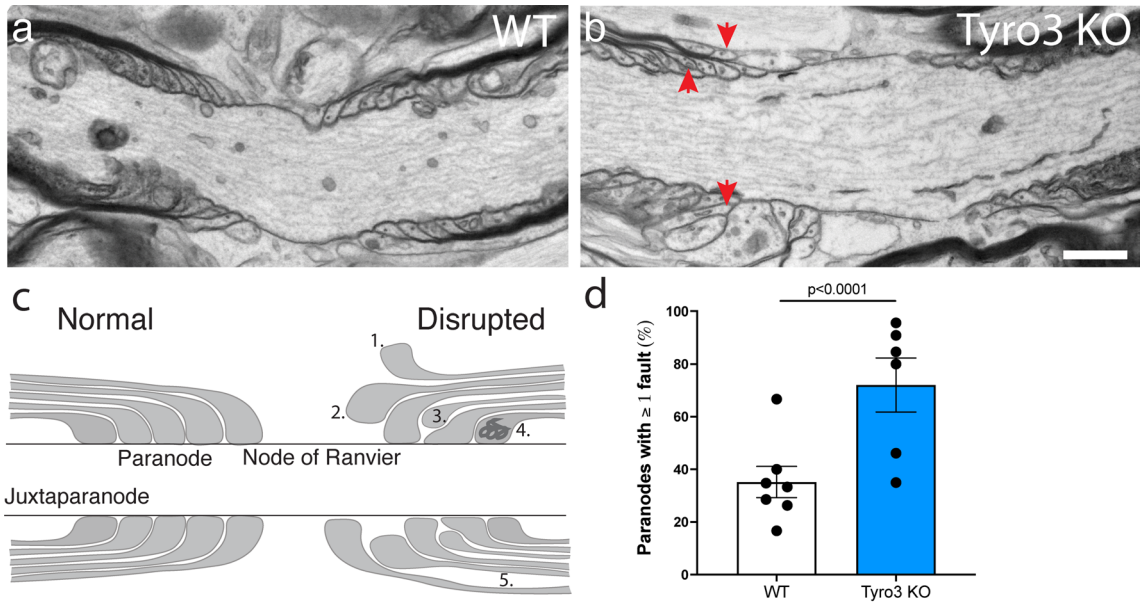

Fig. 1 Tyro3 deficiency is associated with structural abnormalities in paranodes. Representative transmission electron microscopy images from the optic nerve of WT (**a**) and Tyro3 KO (**b**) mice show disrupted paranodal loops in the absence of Tyro3. The number of paranodes with at least one fault was quantified in WT ($n=6$) and Tyro3 KO mice ($n=6$) with paranodes considered disrupted if paranodes displayed at least one of the faults shown in the schematic. Red arrows indicate representative examples of faults. **c** 1. everted loops, 2. detached loops, 3. inverted loops, 4. inclusions, and 5. uncompact myelin, with results shown in (**d**). Tyro3 deletion led to a significant increase in the number of disrupted paranodes ($p<0.0001$). Results are presented as mean ± SEM. Statistical significance was assessed using Chi-square test. Scale bar = 500 nm

paranodes were measured. Deficiency of Tyro3 did not significantly alter the length of the node within either the corpus callosum (Fig. 2b–d; 1.034 ± 0.0049 µm vs. 1.14 ± 0.056 µm WT vs. Tyro3 KO, respectively, $p=0.15$) or the optic nerve (Fig. 2e–g; 1.102 ± 0.044 µm vs. 1.17 ± 0.047 µm WT vs. Tyro3 KO, respectively, $p=0.34$).

Structural changes in myelinated axons are not associated with conduction velocity deficits in the absence of Tyro3

The paranodal disruptions we have identified above, in combination with the previously reported changes to myelin thickness in the CNS of Tyro3 KO mice (Akkermann et al. 2017; Blades et al. 2018), led us to undertake an electrophysiological assessment of electrical conduction within the visual system and corpus callosum of both these groups of mice. We first assessed the latency of CAPs within the lateral horn of the corpus callosum. As the corpus callosum comprises both myelinated and unmyelinated axons, waveforms from this region are composite, with an initial deflection broadly representing large, myelinated axons (N1) and a later deflection representing unmyelinated axons (N2). Representative waveforms from WT and Tyro3 KO mice are shown in Fig. 3b. We found that Tyro3 deficiency did not significantly alter the conduction velocity of either the N1 (Fig. 3c; 0.30 ± 0.015 m/s vs. 0.28 ± 0.019 m/s WT vs. Tyro3 KO respectively, $p=0.41$) or N2 deflection (Fig. 3d; 0.16 ± 0.0062 m/s vs. 0.15 ± 0.0087 m/s WT vs. Tyro3 KO respectively, $p=0.47$). In addition, we measured the half-width of the action potentials for both N1 and N2. We did not observe any statistically significant alteration in the half-width of either N1 (Fig. 3e; 0.27 ± 0.037 ms vs. 0.31 ± 0.41 ms WT vs. Tyro3 KO respectively, $p=0.46$) or N2 (Fig. 3f; 0.56 ± 0.04 ms vs. 0.53 ± 0.07 ms WT vs. Tyro3 KO respectively, $p=0.66$).

We then performed VEPs to assess the visual pathway of the Tyro3 KO and WT mice with light stimulation and implanted electrodes (Fig. 4a, b). We found that VEPs of Tyro3-deficient mice were not significantly different from those of WT mice with no significant alterations in peak response amplitudes of VEP components of the N1 (Fig. 4c; − 112.7 ± 12.85 µV vs. − 152.0 ± 16.43 µV WT vs. Tyro3 KO, respectively, $p=0.07$) or P2 (Fig. 3d; 59.03 ± 14.70 µV vs. 49.73 ± 12.90 µV WT vs. Tyro3 KO, respectively, $p=0.64$). In addition, no significant differences were observed in the latency to reach peak amplitude for the N1 (Fig. 3e; 49.28 ± 1.74 ms vs. 47.13 ± 1.77 ms, WT vs. Tyro3 KO, respectively, $p=0.40$) or P2 responses (Fig. 3f; 80.05 ± 7.36 ms vs. 75.55 ± 5.74 ms, WT vs. Tyro3 KO, respectively, $p=0.64$). Taken together, these data indicate that the absence of Tyro3 did not alter compound action

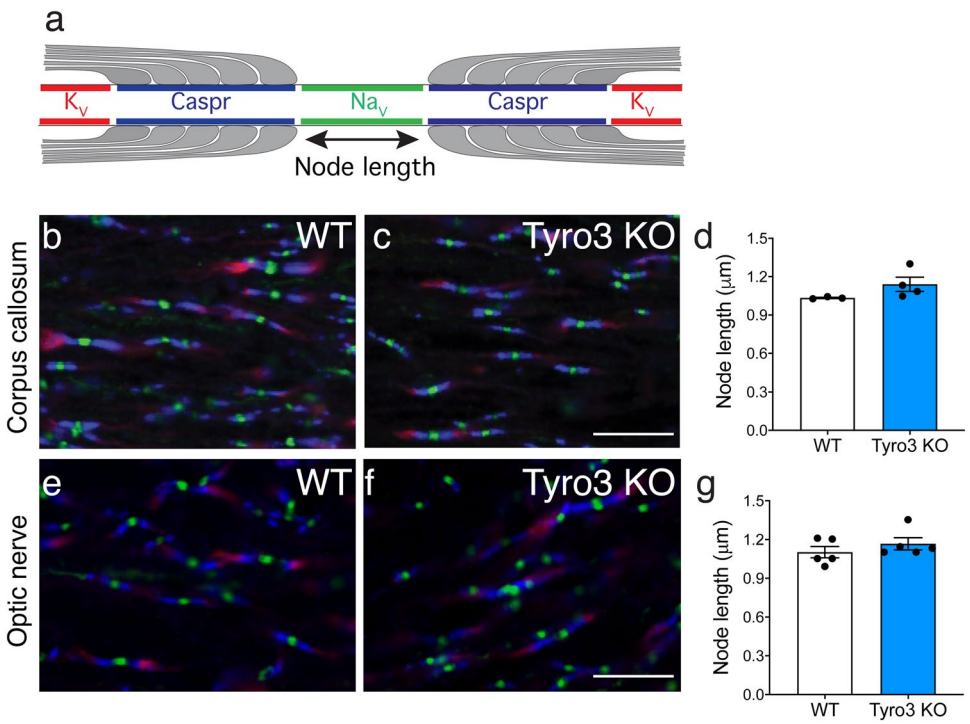

Fig. 2 The length of the node of Ranvier is unaltered in the Tyro3 deficient mouse. **a** Schematic showing the expected localisation of sodium channels (green), Caspr (blue), and potassium channels (red) in the region of the node of Ranvier. Representative images showing labelling of the corpus callosum (**a**, **b**) and the optic nerve (**e**, **f**) with anti-K_V1.2 channels (red), anti-Caspr (blue), and anti-pan-Na_V channels (green). The width of the node (sodium channel reactivity) was measured in both the corpus callosum ($n=3$ WT; $n=4$ Tyro3 KO) and the optic nerve ($n=5$ WT and $n=5$ Tyro3 KO). Nodes and paranodes were not significantly different between genotypes in either the corpus callosum (**d**, **e**) or the optic nerve (**f**, **g**). Numerical results are presented as mean ± SEM, statistical significance was assessed upon width means of mouse using a two-tailed, unpaired Student's *t* test. Scale bar = 10 μm

potential conduction in either the corpus callosum or the visual pathway inclusive of the optic nerve.

Modelling of action potentials predicts that alterations in myelin structure in the Tyro3 KO would result in velocity changes in individual axons but not in the compound action potential

To understand why we failed to identify a substantive change in compound action potential conduction in either the optic nerve or corpus callosum, despite the structural deficits that we identified in the Tyro3 KO mouse, we undertook mathematical modelling using a previously published model of single axon conduction. Numerical values for diameter, g-ratio, lamellae number, and periaxonal space were updated within the model to match myelin parameters in WT mice (Fig. 5a; Table 1). These parameters were then altered to reflect the corresponding myelin alterations measured in the Tyro3 KO mice (Table 1) (Akkermann et al. 2017; Blades et al. 2018). Simulations were performed for a single axon and then for a compound action potential.

In the single axon model, reducing the number of myelin lamellae reduced conduction velocity (Fig. 5). For both the optic nerve and corpus callosum, reducing the number of lamellae by one reduced the conduction velocity by 6–23% (Online Resource 1), depending upon the diameter of the axon (Fig. 5b). Reducing the number of lamellae by two or three produced further reductions in conduction velocity, with the percentage change increasing with each wrap being removed (Fig. 5a). These results are consistent with the previous studies using a single axon (Arancibia-Cárcamo et al. 2017).

Experimental data indicate that WT mice have an average of 5.4 myelin lamellae, whilst Tyro3 KO mice have an average of 4.8 myelin lamellae in the corpus callosum (Table 1). These values cannot be directly modelled in a single axon, because the number of lamellae needs to be a whole number. Similarly, the g-ratio of a single axon will have fixed-sized steps per lamellae when the axon diameter and periaxonal space remain constant. Experimental data indicate that WT mice have an average g-ratio of 0.703, whilst Tyro3 KO mice have an average of 0.727. A reduction of one lamella corresponds to an increase in the *g*-ratio of 0.022 to 0.090, depending on the diameter of the axon, which means that the lower end of the range is consistent with the experimentally observed values for the Tyro3 KO.

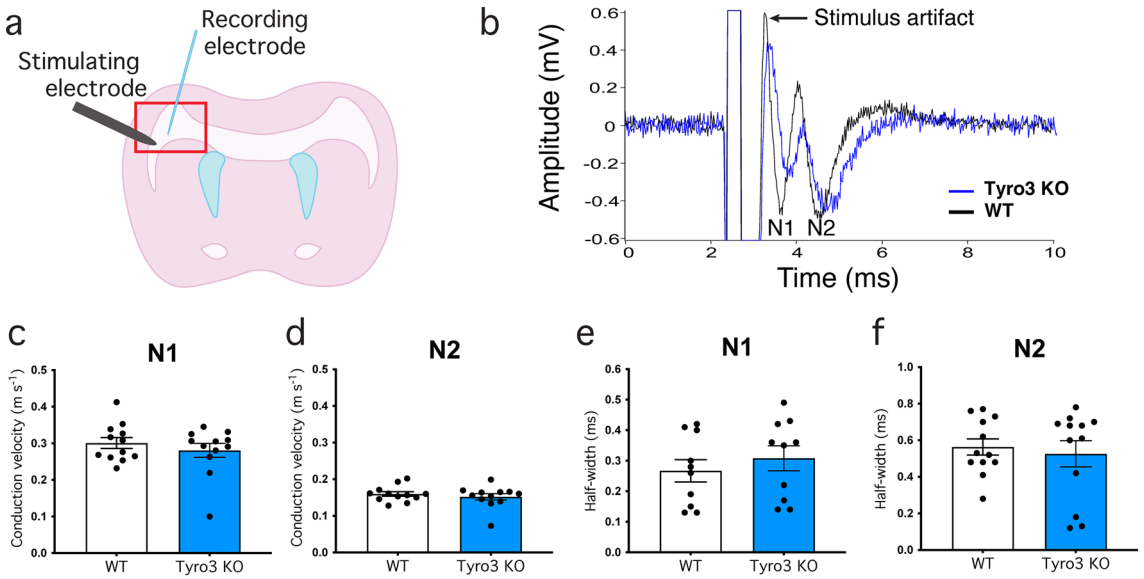

Fig. 3 Compound action potential velocity is not altered in the absence of Tyro3. **a** Schematic diagram showing the position of the stimulating and recording electrodes in the lateral horn of the rostral corpus callosum. Compound action potentials were recorded from WT and Tyro3 KO mice ($n = 12$ per genotype). **b** Representative waveforms from the corpus callosum of WT and Tyro3 KO mice showing N1 and N2 deflections. The peaks of the major deflections N1 and N2 were used to measure the latency of the compound action potentials. No significant differences between genotypes were observed in the latency of either N1 (**c**) or N2 (**d**). Similarly, the loss of Tyro3 did not significantly alter the half-width of either N1 (**e**) or N2 (**f**). Data are presented as mean ± SEM. Statistical significance was assessed using a two-tailed, unpaired Student's t test

Similarly, in the optic nerve, WT mice have an average *g*-ratio of 0.79, whilst Tyro3 KO mice have an average *g*-ratio of 0.81. A reduction of one lamella corresponds to an increase in the *g*-ratio of 0.013–0.058, depending upon the diameter of the axon (Online Resource 1). As the lower end of the range is within the experimentally observed values, the single axon model predicts the Tyro3 KO which should significantly reduce the conduction velocity.

To test how these changes may translate to the function of the integrated system, we also modelled CAPs as a combination of 400 single axons using the experimentally observed values for the WT and Tyro3 KO corpus callosum.

Increasing the average g-ratio in the CAP model produced minor changes in the conduction velocity for the CAP when using the same seed for the random number generators (Fig. 6). Increasing the average *g*-ratio from 0.70 to 0.72 with a corresponding reduction in the number of lamellae 5.4–4.9 resulted in an increased CAP time to peak by less than 2% (Fig. 6a). Therefore, the CAP model predicts the experimentally observed changes due to the deletion of Tyro3 which would not significantly reduce the CAP conduction velocity.

To understand why the change in conduction velocity of the CAP was less than predicted by the single axon, we removed the normal distributions for axon diameter, node lengths, internode lengths, *g*-ratio, and periaxonal space in the CAP model. Removing the normal distribution for these parameters and then decreasing the number of lamellae by 1 produced a significant change of more than 6% in the CAP time to peak (Fig. 6b). This corresponds to the changes in conduction velocity predicted by the single axon model. Further reductions in the number of lamellae produced large reductions in the conduction velocity (Fig. 6b).

Therefore, it appears that normally distributing the parameters of single axons within the CAP model is preventing changes in the myelination of single axons from reducing the conduction velocity of the CAP in our model. To test which parameters are influencing the CAP velocity, we systematically varied the average value for individual parameters (Fig. 6c). At a 10% change in value, the axon diameter had the largest change in time to peak for the CAP (+ 10.2%), followed by g-ratio (+ 8.9%), internode length (− 4.7%), periaxonal space (+ 4.1%), and node length (− 3.5%). However, the experimental data indicate the axon diameter and periaxonal space showed a larger variance than other parameters. Therefore, a change of one standard deviation corresponds to a change of 25% in the model for axon diameter and periaxonal space, but only a 10% change in other parameters. At a 25% change in value, the axon diameter increases the time to peak for the CAP by 27.7% and the periaxonal space increases the time to peak for the CAP by 9.7%. These results indicate that the axon diameter has the largest influence over the conduction velocity of the CAP.

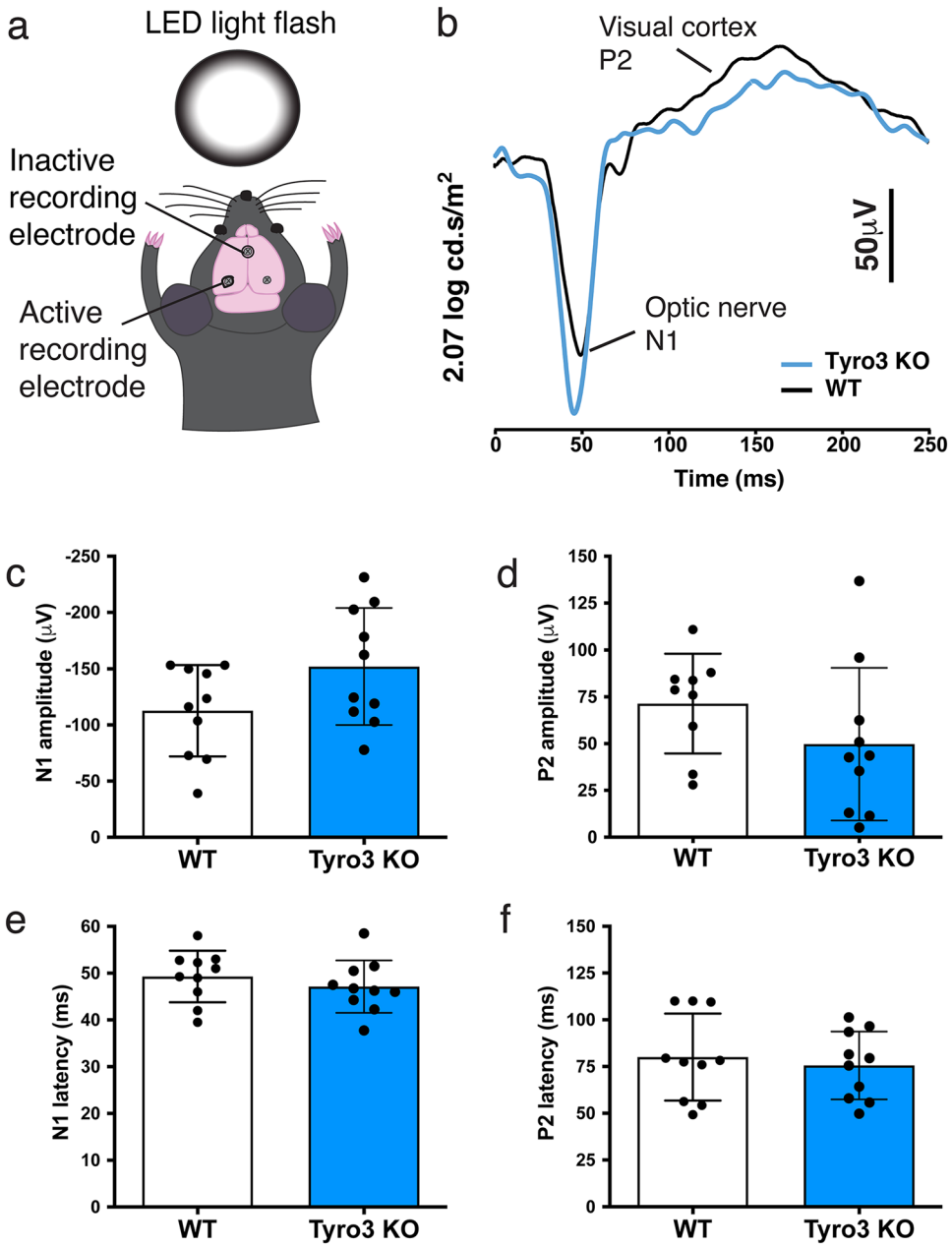

Fig. 4 Tyro3 deletion does not alter visual-evoked potentials. **a** Schematic diagram showing electrode implant positions for VEP recordings. Using high luminous energy flashes, both the amplitude and timing of response to light stimuli from the visual pathway can be measured, inclusive of optic nerve contributions. **b** Combined waveform generated from WT ($n=10$) and Tyro3 KO ($n=10$) mice, showing predominant negative N1, and positive P2 components. We did not observe any significant change in the response amplitude in either the N1 (**c**) or P2 (**d**) in the absence of Tyro3. In addition, we did not observe any alteration to response timing in the N1 (**e**) or P2 (**f**). Data are presented as mean ± SEM. Statistical significance was assessed using a two-tailed, unpaired Student's *t* test

In addition to increasing the time to peak for CAPs, the axon diameter, g-ratio, and periaxonal space increased the CAP half-width by 6.1–30%, with the amount correlating closely with the change in time to peak for the CAP (Fig. 6c). Interestingly, large changes to the g-ratio (greater than 20%) and reduction of the number of lamellae (by 3 wraps or more) produced a second small-amplitude CAP at approximately 30–40 µs. At these large changes, approximately 10% of axons were left with no lamellae in this model, thus becoming unmyelinated axons in the fibre tract, which may also account for the second slower CAP observed in the physiological recording.

The effects of changing the myelination on only large axons were explored (Fig. 6d). The 80 axons (or 20% of 400 axons of the CAP model) with the largest diameter had the number of lamellae reduced by 3. This resulted in less than 2% change in CAP conduction velocity speed. Smaller changes to the number of lamellae and/or smaller percentage of axons had an even smaller effect on the CAP. This demonstrates that significant changes to the myelination of a subset of axons are unlikely to have functional consequences on the CAP.

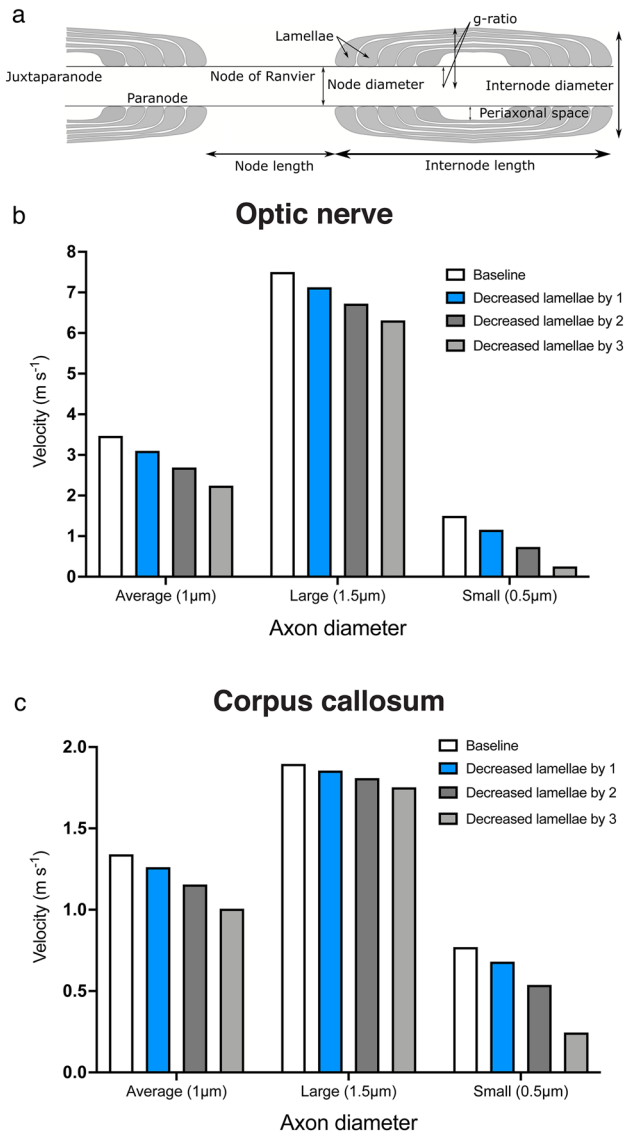

Fig. 5 Single axon model. **a** Schematic diagram of the single axon model and parameters explored. **b** Velocities of action potentials for axons in the optic nerve. The baseline indicates the average parameters for a given axon diameter (average, large or small, as labelled on the *x*-axis). The number of lamellae was then varied as indicated in the legend. **c** Velocities of action potentials for axons in the corpus callosum. The baseline indicates the average parameters for a given axon diameter (average, large or small, as labelled on the *x*-axis). The number of lamellae was then varied as indicated in the legend

Finally, the reproducibility of the CAP data was tested by repeating the simulations 5 times for the WT and Tyro3 KO model, as well as the effect of removing 3 lamellae on 20% of the axons. These repeated simulations were performed without seeding the random number generator to allow for variance in the inputs. We observed very little variance in the CAP generated in these simulations (Online Resource 2), indicating the robustness of our mathematical model.

Discussion

In this study, we used the genetic deletion of Tyro3 in the mouse as a model to study the effect of alterations to myelin structure upon nerve conduction in the CNS. First, we found that, in addition to the previously defined thinner myelin phenotype, Tyro3 KO mice have disrupted paranodal loops in the optic nerve. Conversely, we showed that the length of the node of Ranvier remains unaltered in the absence of Tyro3. In contrast to our expectations, thinner myelin and disordered myelin paranodal loops did not result in slower neuronal conduction in either the corpus callosum or the visual pathway. To understand this unanticipated result, we employed a mathematical model of nerve conduction. This mathematical model predicted that the myelin parameters derived from the Tyro3 KO mouse would result in slower conduction in a single neuron. However, when action potential conduction velocity was modelled for 400 myelinated axons, as a tract, it was predicted that the CAPs in both the optic nerve and corpus callosum would not be significantly altered in the Tyro3 KO mouse.

In the CNS, function is generally considered to be highly correlated with structure. Therefore, as a prelude to assessing conduction velocity in the absence of Tyro3, we first examined the ultrastructure of the nodal and paranodal regions of the optic nerve and corpus callosum. We found that Tyro3 deficiency resulted in substantial disruption to the structure of paranodal axo-glial junctions, although the nodes of Ranvier appeared to be overtly intact. Whilst the loss of the Tyro3 receptor has previously been reported to result in changes to myelin morphology (Miyamoto et al. 2015; Akkermann et al. 2017; Blades et al. 2018), this is the first study to link Tyro3 to altered paranodal integrity. There are multiple proteins known to be involved in the development and maintenance of paranodes including Caspr, contactin, and neurofascin-155, and deleted in colorectal cancer (DCC), amongst others (Einheber et al. 1997; Rios et al. 2000; Tait et al. 2000; Jarjour et al. 2008). Given that the paranode provides points of adherence to the myelin and axonal membranes, it is unsurprising that adherence proteins are critical in the development of paranodes. Of note, Tyro3 is structurally related to adhesion molecules (Lai et al. 1994) and has been shown to participate in platelet aggregation (Zhou et al. 2018). In addition, Gas6, one of the two Tyro3 ligands, has previously been demonstrated to have a role in cell adhesion (McCloskey et al. 1997). It is therefore tempting to speculate that the mechanism underpinning the role of Tyro3 in the paranode involves cell adhesion, potentially

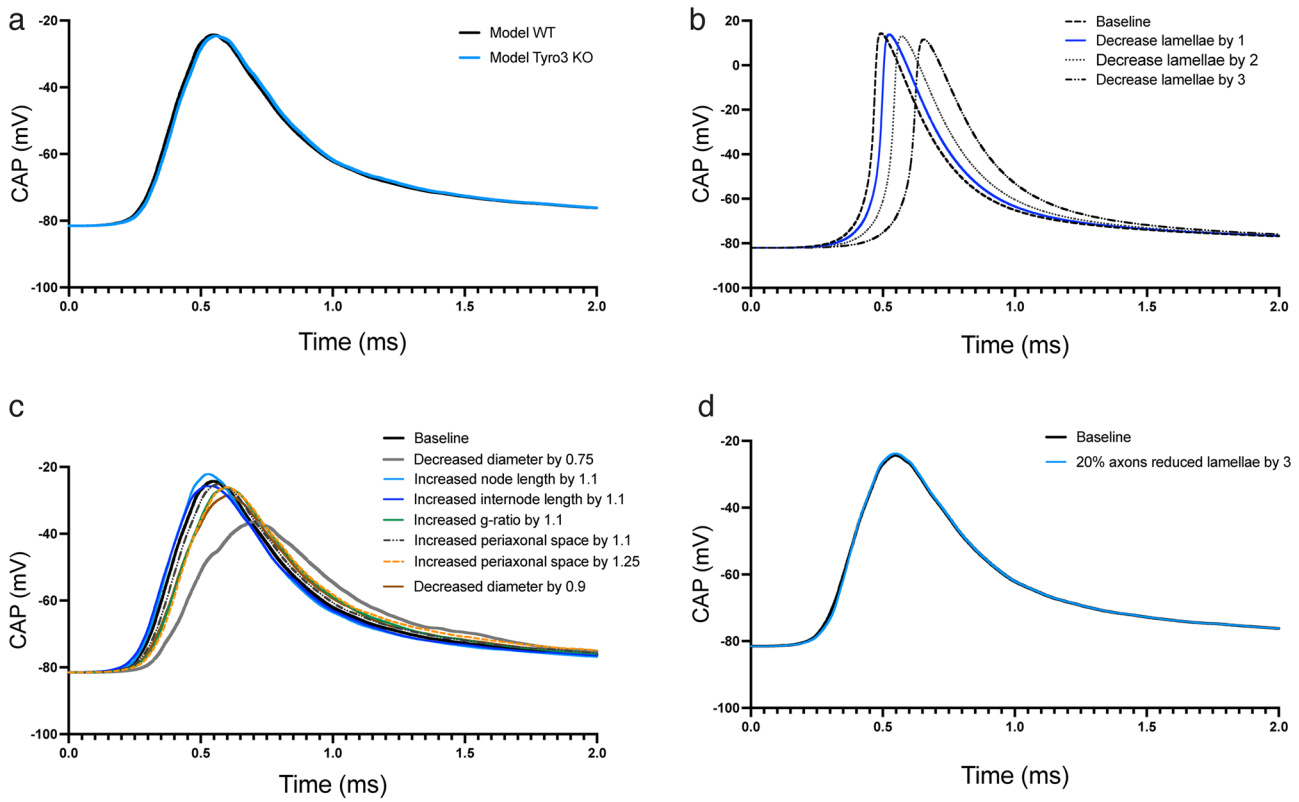

Fig. 6 Compound action potential (CAP) model. The CAP was modelled from 400 single axons. These traces indicate the potential difference recorded 0.75 mm from the site of stimulation. **a** Modelled CAP using experimentally obtained data from WT or Tyro3 KO (**b**). The normal distributions for parameters were removed and the number of lamellae was altered. **c** Changes to the CAP resulting from the systematic variation of baseline parameters as described in the legend. **d** The effects of reducing the number of lamellae on only large axons

through interaction with other paranodal proteins, although this remains to be formally tested.

Based on prior modelling of the influence of myelin thickness on neural conduction velocity (Rushton 1951; Waxman 1980), we expected to observe decreased conduction velocity in the absence of Tyro3, but this was not the case in the corpus callosum or the visual pathway. When CAPs were experimentally measured in the corpus callosum of Tyro3-deficient mice, we found that conduction velocities were normal for both myelinated and unmyelinated axons. Consistent with this, we found that the latency of conduction of VEPs was similar between the Tyro3 deficient and WT mice. To understand these surprising results, we applied a mathematical model in which to explore the predicted contributions of the specific myelin parameters altered in the absence of Tyro3.

Modification of previously described mathematical models (Richardson et al. 2000; Bakiri et al. 2011; Arancibia-Cárcamo et al. 2017) allowed us to explore the effect of structural variations in the myelinated axon, using data derived experimentally from the Tyro3 KO mouse. Applying this model, we found that the reduction in myelin thickness observed in the absence of Tyro3 resulted in slower action potential conductance of single axons when using experimental parameters derived from either the optic nerve or the corpus callosum. In contrast, when these same parameters were used to simulate a population of axons, conduction velocity was not affected, although the width of the CAP was moderately increased by approximately 7% with a reduction of one lamella. It is notable that in our experimental assessment of the half-width of the CAP in the Tyro3 KO mouse, we did observe an increase in the width of the CAP of approximately 15%, although this increase was not statistically significant. Increases to the width of the CAP imply a potential loss of isochronicity, or synchronous arrival of electrical signals at a target. Isochronicity has been shown to be dependent upon myelination in multiple CNS regions, although the exact functional importance of isochronicity has yet to be elucidated (Kimura and Itami 2009).

A deeper exploration of the model revealed that larger changes to myelin thickness than those observed in the Tyro3 KO mouse would be required to produce detectable changes in the CAP in a population of axons. Specifically, an average reduction in the number of lamellae by at least one across all axon diameters was necessary to produce a decrease in the CAP velocity of just under 7%. This consistent decrease

across all axons is not observed in the Tyro3 mouse, where the reduction in myelin thickness was more pronounced on larger calibre axons (Blades et al. 2018), potentially accounting for our inability to identify changes in the latency of the CAP, although this may not be the only or even the major reason why experimentally measured conduction velocity was unaltered in the Tyro3-deficient mouse. We explored the structural parameters individually in our model to test which parameters are determining the properties of the CAP. Consistent with our experimental data, alterations to lengths of nodes had little effect on the CAP velocity. Conversely, varying the axonal diameter had a more profound effect on conduction velocity than myelin thickness. Notably, axon diameter is not altered by the loss of Tyro3 in the CNS (Akkermann et al. 2017; Blades et al. 2018), and thus may be compensating for the myelin changes in this mouse.

What are the biological implications of our findings? As noted above, our data are consistent with the previous studies which show that, following demyelination and repair, conduction velocities recover to pre-demyelination speeds despite the persistence of thinner myelin sheaths (Smith et al. 1979; Heidari et al. 2019). Consistent with the recovery of conduction velocity following remyelination, the function also recovered in these models (Smith et al. 1979; Heidari et al. 2019). Taken together, these data support the hypothesis that remyelination following myelin damage is likely to be beneficial in diseases such as MS and the development of pro-myelinating therapeutics will be clinically and functionally relevant. Importantly, myelin does not need to recover to pre-damage levels to have functional and therapeutic benefits. One benefit of remyelination independent of myelin thickness may in fact be to promote normal axon calibre, which our modelling shows a significant effect on the velocity of the CAP. It has previously been demonstrated that the radial growth of axons is compromised when myelination is disrupted, at least in the PNS (Sherman et al. 2012). Similarly in the CNS, expansion of axon calibre has been linked to signals from oligodendrocytes (Sánchez et al. 1996). As a corollary, it is clear that the assessment of functional outcomes for any given therapeutic intervention is crucial and that myelin changes are a poor predictor of clinical benefit.

Our findings raise the question of whether small or even moderate structural alterations to myelin alter functional outcomes. This is particularly relevant for considering the effects of myelination in response to neuronal activity, also known as activity-dependent myelination. It is postulated that activity-dependent myelination in the adult is a form of myelin plasticity whereby the increased activity of a neuron in response to learning or motor tasks results in increased myelin deposition on that neuron, ultimately changing conductivity. The myelin deposition can take the form of either new internodes on an already myelinated axon or even on a previously unmyelinated axon (Wake et al. 2015; Mitew et al. 2018). Alternatively, the structure of an existing myelin internode can be altered, for example by extending the length or increasing the thickness of an internode, although this is yet to be formally linked to neuronal activity (Dutta et al. 2018). New myelin internodes or structural changes have been hypothesised to increase conduction velocity and thus optimise neuronal signalling. However, the proposed conductivity changes are often theoretical, with only a handful of structural myelin studies providing a link to downstream, functional outcomes (McKenzie et al. 2014; Gibson et al. 2014). Our new data highlight the importance of taking an experimental approach to formally link myelin alterations to conductivity changes, and that it is important to distinguish between conductivity changes in a single neuron versus neural tracts. Here, it is important to acknowledge in this study we have only explored highly myelinated brain regions, and that an increase in myelination in a relatively unmyelinated region such as the cortex may have a more significant effect. In addition, our data may indirectly provide support for the idea that, in the absence of any meaningful change in conduction-based parameters, the main role of activity-dependent myelination is potentiated metabolic coupling of axons to oligodendrocytes (Fünfschilling et al. 2012; Lee et al. 2012).

Conclusions

We have identified a novel role for Tyro3 in myelin paranodal loop integrity that, together with the known reduction in myelin thickness, makes the Tyro3 deficient mouse a useful model for exploring the functional outcomes of myelin modifications. Our experimental assessments of action potential conduction in the Tyro3 KO mouse unexpectedly failed to identify significant electrophysiological changes in either the visual pathway or the corpus callosum at the level of the CAP. Using mathematical modelling of conduction, we explored the theoretical effect of myelin changes upon axonal conduction. We conclude that, whilst changes to myelin thickness and paranodal structure are likely to result in significant changes in the conduction of action potentials in single neurons, they do not necessarily lead to large-scale differences in conduction in white matter tracts. Exploration of our model predicts that an average reduction in myelin thickness of at least two lamellae is required to impact the velocity and shape of the CAP. Taken together, our data highlight the importance of adopting an experimental approach to assessing functional outcomes of changes observed in myelin structure.

Supplementary Information The online version contains supplementary material available at https://doi.org/10.1007/s00429-022-02489-8.

Acknowledgements Funding for this project was provided by The Trish Multiple Sclerosis Research Foundation to TJK and MB (17–0216), as well as an Australian Research Council Linkage Grant to CTON and BB (LP160100126). FB was supported by the Australian Government Research Training Program Scholarship. JDC was supported by the Australian Research Council Industrial Transformation Training Centre in Cognitive Computing for Medical Technologies (project number ICI70200030). CTON was supported by a Melbourne Research Fellowship. TJK was supported by an Investigator grant from the NH&MRC (#APP1175775). The Florey Institute of Neuroscience and Mental Health acknowledges the support received from the Victorian Government, in particular, the funding from the Operational Infrastructure Support Grant. We thank the Florey Neuroscience Microscopy Facility and the Centre for Advanced Histology & Microscopy (CAHM) at the Peter MacCallum Cancer Centre (Parkville, VIC, AU) for technical assistance.

Author contributions: Trevor J. Kilpatrick and Michele D. Binder designed research. Farrah Blades., Jordan D. Chambers, Timothy D. Aumann, Christine T.O. Nguyen, Vickie H.Y. Wong performed research. Farrah Blades., Jordan D. Chambers, Timothy D. Aumann, Christine T.O. Nguyen, Vickie H.Y. Wong, Andrea Aprico, Eze C. Nguyen, Bang V. Bui, David B. Grayden, Michele D. Binder analysed data. Farrah Blades., Jordan D. Chambers and Michele D. Binder wrote the paper.

Funding Funding for this project was provided by The Trish Multiple Sclerosis Research Foundation to TJK and MB (17-0216), as well as an Australian Research Council Linkage Grant to CTON and BB (LP160100126). FB was supported by the Australian Government Research Training Program Scholarship. JDC was supported by the Australian Research Council Industrial Transformation Training Centre in Cognitive Computing for Medical Technologies (project number ICI70200030). CTON was supported by a Melbourne Research Fellowship. TJK was supported by an Investigator grant from the NH&MRC (#APP1175775). The Florey Institute of Neuroscience and Mental Health acknowledges the support received from the Victorian Government, in particular, the funding from the Operational Infrastructure Support Grant.

Data availability The code/software described in the paper will be freely available online at https://github.com/JordanChambers/compound-action-potential upon publication of this manuscript.

Declarations

Conflicts of interest/competing interests The authors have no relevant financial or non-financial interests to disclose.

Ethics approval All animal procedures were performed in accordance with the approval of the Florey Institute of Neuroscience animal ethics committee and in accordance with the National Health and Medical Research Council (Australia) guidelines.

Consent to participate Not applicable.

Consent for publication Not applicable.

References

Akkermann R, Aprico A, Perera AA et al (2017) The TAM receptor Tyro3 regulates myelination in the central nervous system. Glia 65:581–591. https://doi.org/10.1002/glia.23113

Arancibia-Cárcamo IL, Ford MC, Cossell L et al (2017) Node of Ranvier length as a potential regulator of myelinated axon conduction speed. Elife 6:e23329. https://doi.org/10.7554/elife.23329

Bakiri Y, Káradóttir R, Cossell L, Attwell D (2011) Morphological and electrical properties of oligodendrocytes in the white matter of the corpus callosum and cerebellum. J Physiol 589:559–573. https://doi.org/10.1113/jphysiol.2010.201376

Blades F, Aprico A, Akkermann R et al (2018) The TAM receptor TYRO3 is a critical regulator of myelin thickness in the central nervous system. Glia 66:2209–2220. https://doi.org/10.1002/glia.23481

Bull S-J, Bin JM, Beaumont E et al (2014) Progressive disorganization of paranodal junctions and compact myelin due to loss of DCC expression by oligodendrocytes. J Neurosci 34:9768–9778. https://doi.org/10.1523/jneurosci.0448-14.2014

Chang K-J, Redmond SA, Chan JR (2016) Remodeling myelination: implications for mechanisms of neural plasticity. Nat Neurosci 19:190–197. https://doi.org/10.1038/nn.4200

Duncan ID, Marik RL, Broman AT, Heidari M (2017) Thin myelin sheaths as the hallmark of remyelination persist over time and preserve axon function. Proc Natl Acad Sci 114:E9685–E9691. https://doi.org/10.1073/pnas.1714183114

Dutta DJ, Woo DH, Lee PR et al (2018) Regulation of myelin structure and conduction velocity by perinodal astrocytes. Proc Natl Acad Sci 115:11832–11837. https://doi.org/10.1073/pnas.1811013115

Einheber S, Zanazzi G, Ching W et al (1997) The axonal membrane protein caspr, a homologue of neurexin IV, is a component of the septate-like paranodal junctions that assemble during myelination. J Cell Biol 139:1495–1506. https://doi.org/10.1083/jcb.139.6.1495

Fünfschilling U, Supplie LM, Mahad D et al (2012) Glycolytic oligodendrocytes maintain myelin and long-term axonal integrity. Nature 485:517–521. https://doi.org/10.1038/nature11007

Gibson EM, Purger D, Mount CW et al (2014) Neuronal activity promotes oligodendrogenesis and adaptive myelination in the mammalian brain. Science 344:1252304. https://doi.org/10.1126/science.1252304

Halter JA, Clark JW (1991) A distributed-parameter model of the myelinated nerve fiber. J Theoret Biol 148:345–382. https://doi.org/10.1016/s0022-5193(05)80242-5

Heidari M, Radcliff AB, McLellan GJ et al (2019) Evoked potentials as a biomarker of remyelination. Proc Natl Acad Sci 116:27074–27083. https://doi.org/10.1073/pnas.1906358116

Hodgkin AL, Huxley AF (1952) A quantitative description of membrane current and its application to conduction and excitation in nerve. J Physiol 117:500–544. https://doi.org/10.1113/jphysiol.1952.sp004764

Holder GE (2004) Electrophysiological assessment of optic nerve disease. Eye 18:1133–1143. https://doi.org/10.1038/sj.eye.6701573

Huxley AF, Stämpfli R (1949) Evidence for saltatory conduction in peripheral myelinated nerve fibres. J Physiol 108:315–339. https://doi.org/10.1111/(issn)1469-7793

Jarjour AA, Bull S-J, Almasieh M et al (2008) Maintenance of axo-oligodendroglial paranodal junctions requires DCC and Netrin-1. J Neurosci 28:11003–11014. https://doi.org/10.1523/jneurosci.3285-08.2008

Kimura F, Itami C (2009) Myelination and isochronicity in neural networks. Front Neuroanat 3:12. https://doi.org/10.3389/neuro.05.012.2009

Lai C, Gore M, Lemke G (1994) Structure, expression, and activity of Tyro 3, a neural adhesion-related receptor tyrosine kinase. Oncogene 9:2567–2578

Lee Y, Morrison BM, Li Y et al (2012) Oligodendroglia metabolically support axons and contribute to neurodegeneration. Nature 487:443–448. https://doi.org/10.1038/nature11314

Lubetzki C, Sol-Foulon N, Desmazières A (2020) Nodes of Ranvier during development and repair in the CNS. Nat Rev Neurol 16:426–439. https://doi.org/10.1038/s41582-020-0375-x

McCloskey P, Fridell Y-W, Attar E et al (1997) GAS6 mediates adhesion of cells expressing the receptor tyrosine kinase Axl. J Biol Chem 272:23285–23291. https://doi.org/10.1074/jbc.272.37.23285

McKenzie IA, Ohayon D, Li H et al (2014) Motor skill learning requires active central myelination. Science 346:318–322. https://doi.org/10.1126/science.1254960

Mitew S, Gobius I, Fenlon LR et al (2018) Pharmacogenetic stimulation of neuronal activity increases myelination in an axon-specific manner. Nat Commun 9:306. https://doi.org/10.1038/s41467-017-02719-2

Miyamoto Y, Torii T, Takada S et al (2015) Involvement of the Tyro3 receptor and its intracellular partner Fyn signaling in Schwann cell myelination. Mol Biol Cell 26:3489–3503. https://doi.org/10.1091/mbc.e14-05-1020

Richardson AG, McIntyre CC, Grill WM (2000) Modelling the effects of electric fields on nerve fibres: Influence of the myelin sheath. Med Biol Eng Comput 38:438–446. https://doi.org/10.1007/bf02345014

Rios JC, Melendez-Vasquez CV, Einheber S et al (2000) Contactin-associated protein (Caspr) and contactin form a complex that is targeted to the paranodal junctions during myelination. J Neurosci 20:8354–8364. https://doi.org/10.1523/jneurosci.20-22-08354.2000

Rushton WAH (1951) A theory of the effects of fibre size in medullated nerve. J Physiol 115:101–122

Sánchez I, Hassinger L, Paskevich PA et al (1996) Oligodendroglia regulate the regional expansion of axon caliber and local accumulation of neurofilaments during development independently of myelin formation. J Neurosci 16:5095–5105. https://doi.org/10.1523/jneurosci.16-16-05095.1996

Schindelin J, Arganda-Carreras I, Frise E et al (2012) Fiji: an open-source platform for biological-image analysis. Nat Methods 9:676–682. https://doi.org/10.1038/nmeth.2019

Sherman DL, Krols M, Wu L-MN et al (2012) Arrest of myelination and reduced axon growth when schwann cells lack mTOR. J Neurosci 32:1817–1825. https://doi.org/10.1523/jneurosci.4814-11.2012

Smith KJ, Blakemore WF, McDonald WI (1979) Central remyelination restores secure conduction. Nature 280:395–396

Tait S, Gunn-Moore F, Collinson JM et al (2000) An Oligodendrocyte cell adhesion molecule at the site of assembly of the paranodal axo-glial junction. J Cell Biolo 150:657–666. https://doi.org/10.1083/jcb.150.3.657

Vidal-Jordana A, Rovira A, Arrambide G et al (2021) Optic nerve topography in multiple sclerosis diagnosis: the utility of visual evoked potentials. Neurology 96:e482–e490. https://doi.org/10.1212/wnl.0000000000011339

Wake H, Ortiz FC, Woo DH et al (2015) Nonsynaptic junctions on myelinating glia promote preferential myelination of electrically active axons. Nat Commun 6:7844. https://doi.org/10.1038/ncomms8844

Waxman SG (1980) Determinants of conduction velocity in myelinated nerve fibres. Muscle Nerve 3:141–150. https://doi.org/10.1002/mus.880030207

Waxman SG, Bennett MVL (1972) Relative conduction velocities of small myelinated and non-myelinated fibres in the central nervous system. Nat New Biol 238:217–219. https://doi.org/10.1038/newbio238217a0

Zhou J, Yang A, Wang Y et al (2018) Tyro3, Axl, and Mertk receptors differentially participate in platelet activation and thrombus formation. Cell Commun Signal 16:98. https://doi.org/10.1186/s12964-018-0308-0